Planar Multilayer Circuit Quantum Electrodynamics

Z. K. Minev,* K. Serniak, I. M. Pop,‡ Z. Leghtas, K. Sliwa, M. Hatridge, L. Frunzio, R. J. Schoelkopf, and M. H. Devoret†

Department of Applied Physics, Yale University, New Haven, Connecticut 06511, USA

(Received 7 September 2015; revised manuscript received 2 March 2016; published 29 April 2016)

Experimental quantum information processing with superconducting circuits is rapidly advancing, driven by innovation in two classes of devices, one involving planar microfabricated (2D) resonators, and the other involving machined three-dimensional (3D) cavities. We demonstrate that circuit quantum electrodynamics can be implemented in a multilayer superconducting structure that combines 2D and 3D advantages. We employ standard microfabrication techniques to pattern each layer, and rely on a vacuum gap between the layers to store the electromagnetic energy. Planar qubits are lithographically defined as an aperture in a conducting boundary of the resonators. We demonstrate the aperture concept by implementing an integrated, two-cavity-mode, one-transmon-qubit system.

DOI: 10.1103/PhysRevApplied.5.044021

I. INTRODUCTION

Circuit quantum electrodynamics (cQED) [1,2], based on the interactions of superconducting qubits with microwave light, is currently emerging as one of the most promising experimental platforms for quantum information processing [3,4] and quantum optics experiments [5–8]. In these superconducting circuits, Josephson junctions provide the nonlinearity for qubits, while low-loss microwave resonators provide linear processing functions for quantum memories [9–12], readout or entanglement buses [13,14], and filtering [15,16].

Circuit QED has been developed in two platforms: fully planar (2D) circuits, which benefit from the geometric precision and parallel production of established microfabrication technologies, and 3D circuits involving conventionally machined cavities, but with superior coherence times. Through improved design and material optimization, 2D qubits and resonators have significantly progressed, with internal quality factors (Q_i) exceeding 10^6 (Refs. [17–21]). On the other hand, 3D resonators store a larger fraction of their electromagnetic energy in vacuum, making them less susceptible to material imperfections, and can reach $Q_i > 10^8$ (Refs. [11,22]). Can a new cQED design take advantage of the benefits of both 2D and 3D platforms?

We propose to lithographically pattern qubits and resonators in multiple planes separated by vacuum gaps used to store the electromagnetic energy. Thin-film aluminum resonators built in this multilayer planar way recently demonstrated low losses ($Q_i > 3 \times 10^6$) at the single photon level [23]. One of the main challenges in the implementation of a multilayer approach to cQED is the design of qubit-resonator coupling between different layers of a structure.

In the 2D and 3D platforms, coupling is achieved by inserting the qubit metallic structure onto the insulating region of the resonator. In a perturbative description of the coupling, the electric field of the resonator mode is aligned with the electric dipole of the qubit mode [Fig. 1(a)]. However, in a multilayer architecture, this method would require fabricating qubits perpendicular to the lithographic planes. We propose a different design strategy in which the qubit design layer coincides with one of the lithographic

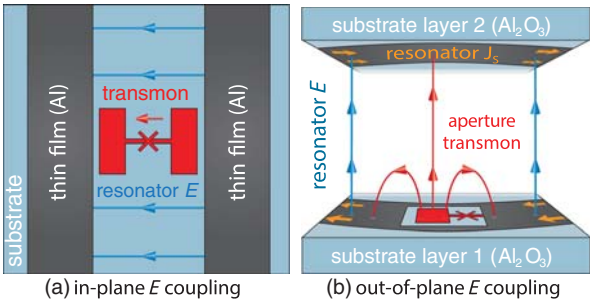

(a) in-plane E coupling (b) out-of-plane E coupling

FIG. 1. Qubit-resonator coupling in different cQED approaches. (a) In-plane coupling in 2D. The electric field lines of the resonator (blue) are aligned with the dipole moment of the qubit (red), both of which are in the plane of qubit fabrication. (b) Out-of-plane coupling in a multilayer planar device. The resonator is now represented as a section of a multilayer whispering-gallery-mode resonator [23], consisting of two superconducting thin-film rings deposited on different sapphire substrates that are separated by an electrically thin vacuum gap. The qubit is defined by an aperture carved directly from the conducting boundary of the resonator. The orange and blue arrows represent the resonator surface-current density and electric field lines, respectively.

*Corresponding author.
zlatko.minev@yale.edu
†Corresponding author.
michel.devoret@yale.edu
‡Present address: Physikalisches Institut, Karlsruhe Institute of Technology, 76131 Karlsruhe, Germany.

planes. It uses out-of-plane fields to couple the qubit—which we nickname aperture transmon—to the resonator mode [Fig. 1(b)].

To demonstrate the feasibility and advantages of our multilayer planar platform for cQED, we present in this paper the implementation and coherence properties of an integrated system composed of two standing modes coupled to a qubit, a now-standard configuration for many basic cQED experiments [6,8,24–26]. Our implementation is based on the two TEM modes of a superconducting whispering-gallery (WG) resonator introduced in Ref. [23]. One of the modes is overcoupled ($Q = 10^4$) to a readout amplification chain, while the other is maintained as high Q as possible ($Q = 2 \times 10^6$). Both modes couple to a transmon qubit [27] with a $T_1 = 70$ μs lifetime. The Hamiltonian of this device [see Eq. (A1)] is similar to that of the 3D device in Ref. [6], and can be used for the implementation of cavity-based error-correction protocols [10].

II. DEVICE AND METHODS

Figure 2 shows the multilayer chip-stack elements of the measured device. Two sapphire chips serve as substrates for each of the two Al patterned rings. We position the chips with the rings aligned inside an Al sample holder to establish the boundary conditions of the TEM modes of the WG resonator. Machined ledges in the sample holder maintain a vacuum gap of 100 μm between the chips (details of the assembly can be found in the Appendix A). The two orders of magnitude in aspect ratio between the mode wavelength and the stack gap spacing ensure tight confinement of the fields of the modes. In particular, the inductive participation ratio of the sample holder is found to be 10^{-8} or smaller for each of the modes, as computed with

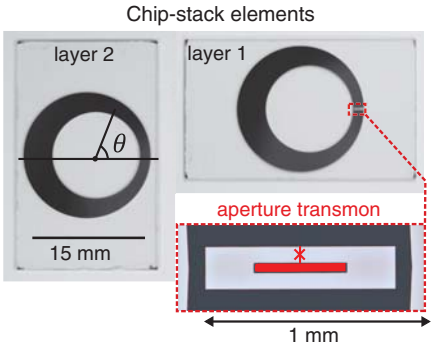

FIG. 2. Photograph of chip-stack elements. Thin-film Al rings are patterned in a single *e*-beam lithography step along with the Josephson junction on a sapphire substrate. The boxed region shows a magnified optical micrograph of the embedded aperture qubit (false colored in red) and the location of the Josephson junction (red cross). The axis of symmetry, represented over substrate layer 2, defines the angular position θ around the ring.

HFSS [28] finite-element model, assuming a London penetration depth of 50 nm.

The transmon qubit is directly patterned in the thin film of the ring in layer 1, as shown in the inset of Fig. 2. The qubit consists of a 0.05×0.5 mm island inside a 0.23×1 mm aperture in the ring, connected through a Josephson junction with $E_J/h = 12$ GHz. The qubit structure perturbs the resonator mode frequencies only at the percent level. The island nominally shares 60 fF of capacitance with its own ring and 5 fF with the opposite ring. The junction capacitance and these geometric capacitances define the nominal qubit charging energy $E_C/h = 275$ MHz, frequency $\omega_q/2\pi = 4.85$ GHz, anharmonicity $\alpha = 320$ MHz [27]. The rings and the qubit are fabricated simultaneously in a single electron-beam lithography step using a double-angle, bridge-free technique [29,30].

The spatial mode orthogonality of the two WG modes allows us to implement the long-lived storage ($D^{\perp}$) and overcoupled readout ($D^{\parallel}$) modes of a quantum register within the same physical structure. In the following, we refer to these two modes simply as "storage" and "readout," with nominal coupling $Q_c^S > 10^8$ and $Q_c^R = 1.8 \times 10^4$ (see Appendix A), respectively.

The sample holder is thermally anchored to the base stage of a dilution unit at 15 mK. We used the standard cQED measurement setup (see Appendix B) with the addition of a phase-preserving, quantum-limited, Josephson parametric amplifier [31].

III. PLANAR-TO-NONPLANAR COUPLING

For dispersive coupling between a transmon qubit (q) and a resonator mode (r), the strength of the cross-Kerr χ_{qr} depends primarily on the detuning $\Delta = \omega_r - \omega_q$, aperture geometry, and the resonator fields at its position. In order to quantify the aperture coupling independently of the potentially tunable Δ, we define the effective coupling rate $g_{qr} = \Delta\sqrt{\chi_{qr}(\Delta)/E_C}$ [27], which is approximately independent of Δ and E_J in the transmon limit $E_J/E_C \gg 1$ and for weak interaction $g \ll \Delta$.

In 2D and 3D, the coupling strength g can be understood as arising from an interaction between the bare electric field of the resonator and the electric-dipole-like charge distribution of the qubit. Here, in our multilayer structure where the qubit is patterned in an aperture in one of the layers, the coupling mechanism is more involved. Figures 3(b) and 3(c) show the charge and current distribution of the qubit mode, respectively. The coupling is determined by the overlap between these distributions and those of the resonator mode.

The interplay of the capacitive (charge overlap) and inductive (current overlap) coupling is shown in Fig. 3(d), where we plot the dependence of g on the qubit position θ (see Appendix E) for the simulation procedure based on

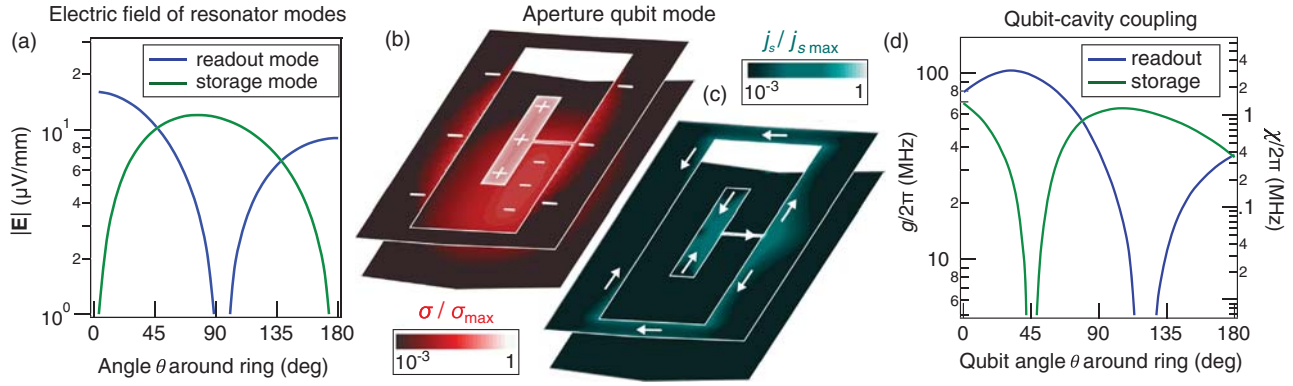

FIG. 3. Electric and magnetic contributions to qubit-resonator coupling, as calculated using a HFSS. (a) Electric field amplitude $|\mathbf{E}|$ in the resonator WG modes as a function of θ, for one photon of energy. The angular dependence of the surface-current-density j_s follows that of E, but is shifted by 90°. (b) Surface-charge-density amplitude σ shown in color scale with overlayed white signs to indicate the relative charge polarity. The charges in the island and corresponding image charges in the opposite layer below determine the electric contribution to the qubit-resonator coupling. (c) Qubit-mode surface-current amplitude j_s shown in color scale with overlayed white arrows to represent the direction of the flow. The narrow rails on each side of the aperture are equivalent to a shared inductance between the qubit and resonator and determine the magnetic contribution to the qubit-resonator coupling. (d) Qubit-resonator coupling rate g of the aperture qubit to the WG resonator modes as a function of the qubit position around the ring θ. The right vertical axis also shows the equivalent cross-Kerr χ for a $\Delta = 1$ GHz detuning. The coupling g is the algebraic sum of the electric and magnetic contributions, which interfere constructively or destructively as a function of θ. For the readout (storage), maximal constructive (destructive) interference occurs at about 45°, while near $\theta = 0$, 180° the coupling is capacitive (inductive).

black-box circuit quantization [32]. Varying the position θ of the transmon varies its coupling g to the resonator, independently of its frequency and anharmonicity. For a given position θ, g can be further adjusted by changing the dimensions of the aperture.

IV. EXPERIMENTAL RESULTS

Microwave spectroscopy revealed the transmon qubit, storage ($D^{\perp}$), and readout ($D^{\parallel}$) modes at 4.890, 7.070, and 7.267 GHz, respectively, in 1% agreement with the HFSS numerical simulations of the sample [33]. From qubit spectroscopy, we observed a transmon anharmonicity of 310 MHz, in 5% agreement with the nominal qubit charging energy [27].

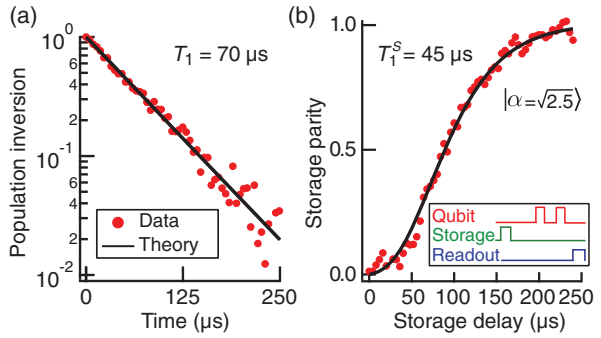

FIG. 4. (a) Aperture transmon energy relaxation. A single exponential fits the data with a $T_1 = 70$ μs. The population inversion is defined as $(P_e - P_e^{\rm th})/(P_g^{\rm th} - P_e^{\rm th})$, where $P_e^{\rm th}$ and $P_g^{\rm th}$ are the thermal populations. (b) Storage parity relaxation from which we infer an energy relaxation lifetime of $T_1^S = 45$ μs. Inset: pulse sequence for the measurement, see Appendix D.

Figure 4(a) shows the qubit free decay with an exponential time constant $T_1 = 70$ μs. We measured $T_2^R = 8$ μs and $T_2^E = 20$ μs. The dephasing noise was measured by a Carr-Purcell-Meiboom-Gill (CPMG) technique (see Fig. 6). The contributions to the dephasing noise are not currently understood; they could be the result of photon shot noise [34], mechanical vibrations, and/or offset charge drifts [27]. The readout linewidth $\kappa_r/2\pi = 0.35$ MHz and qubit dispersive shift $\chi_{qr}/2\pi = 0.30$ MHz agree to 10% with simulations.

From spectroscopy of the storage at photon number $\bar{n} \approx 10^2$, we measure a linewidth $\Delta\omega_S/2\pi = 4$ kHz which includes self-Kerr broadening in addition to dephasing. From this linewidth, we infer an approximate lower bound on the storage coherence time: $T_2^S \gtrsim 2/\Delta\omega_S = 80$ μs.

To measure the storage lifetime T_1^S in the single-photon regime [see Fig. 4(b)], we use the photon-number parity protocol introduced in Refs. [6,25,35], which, in our case, is more sensitive than a direct-amplitude decay measurement. A Gaussian pulse of 1 μs duration first displaces the storage cavity to a coherent state with $\bar{n} = 2.5$ photons, a state with essentially zero parity $P_s = \langle \exp(-i\pi a^\dagger a)\rangle = 5 \times 10^{-3}$, where a is the storage lowering operator. After a variable delay, a Ramsey-like sequence with a fixed time delay of π/χ_{qs} maps the parity of the storage photon number to the qubit state. From the parity measurement, we extracted a low-photon number $T_1^S = 45$ μs. Measurements at higher photon numbers (up to $\bar{n} = 200$) showed no power dependence of T_1^S. The calibrations needed for this protocol are described in Appendix D.

TABLE I. Main parameters of the sample. The cross-Kerr interaction with the qubit mode is denoted χ_q, while α denotes anharmonicity. All parameters are measured except the storage and readout anharmonicity, which are calculated from $\alpha_{s,r} = \chi^2_{qs,r}/4\alpha_q$ [32]. The symbol * indicates a Gaussian decay.

Mode	Qubit	Storage	Readout
Frequency (GHz)	4.890	7.070	7.267
T_1 (μs)	70	45	0.42
$T_2 \vert T_2^{\mathrm{E}}$ (μs)	$8^\star \vert 20$	$\gtrsim 80$	$\cdots$
$\alpha/2\pi$ (MHz)	310	1×10^{-4}	1.5×10^{-4}
$\chi_q/2\pi$ (MHz)	$\cdots$	0.25	0.30

V. DISCUSSION

We summarize the two-cavity-mode, one-qubit device interaction strengths, and lifetimes in Table I. The measured frequencies and coupling energies of the multilayer device agree at the percent and ten-percent level, respectively, with design values from numerical simulations. The discrepancy can be explained by machining tolerances (25 μm) of the gap spacing and chip alignment in the sample holder, and could be improved by using micromachined separators to support the structure [36–38].

The measured coherence times are on par with those of two-cavity, one-qubit devices using 3D rectangular cavities [6,8,25,26,35,39]. The qubit and storage lifetimes are not limited by their input-output (I-O) coupling (see Appendix C 3). These lifetimes could be extended by design optimization, as well as material advances demonstrated in the 2D and 3D architectures [11,17,18,21,40,41]. Spurious fringing fields in the substrates and environment would be reduced by decreasing the gap spacing and improving the chip-stack alignment. In the present device, the vacuum gap of 100-μm captures ~90% of the cavity energy and 15% of the qubit energy in the vacuum. A decrease in the gap by a factor of 10 would, for both modes, decrease the bulk dielectric participation down to the percent level, a gain of more than one order of magnitude over planar and 3D qubits, provided that we would not be limited by the surface quality of the superconducting film.

We demonstrate at least three orders of magnitude separation in I-O coupling Q between the storage and readout, which not only share the same physical footprint, but differ by only 200 MHz in frequency. This type of spatial mode control is advantageous when dealing with cross talk and frequency crowding in devices with increased complexity.

The measured device is a suitable candidate for a quantum register [10,42], with storage coherence time $T_2^S = 80$ μs exceeding that of the qubit by an order of magnitude. The storage could provide a large Hilbert space to encode quantum information, while the long-lived qubit serves as a conditional, nonlinear control over the cavity space with a low bit-flip error rate.

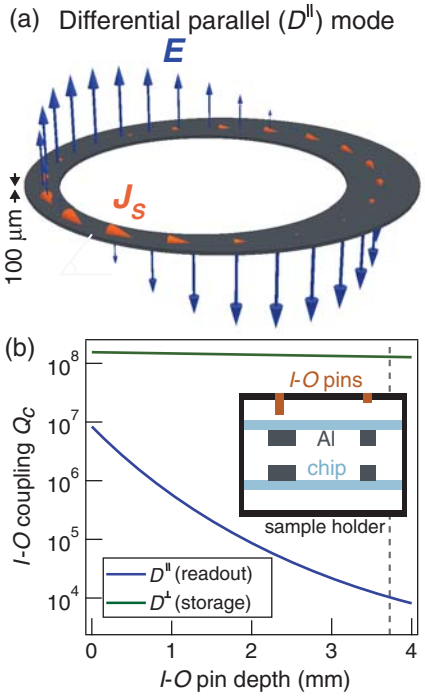

FIG. 5. (a) HFSS calculation of the surface currents and electric fields, which are contained within the 100-μm vacuum gap separating the two layers, for the TEM $D^{\parallel}$ WG mode. The orthogonal $D^{\perp}$ mode closely resembles the $D^{\parallel}$, up to a 90° rotation. Depending on the configuration of the input-output (I-O) coupling pins [see (c)], these modes can be used either as a qubit readout mode (low coupling-quality-factor Q_c) or storage for quantum states (high Q_c). (b) Simulated Q_c as a function of the coupling coax pin depth inside the sample holder at $\theta = 0°$. The inset shows a not-to-scale cross-sectional representation of the chip stack in a sample holder (black). We can selectively couple to $D^{\parallel}$ ($Q_c^R = 10^4$) while remaining uncoupled from $D^{\perp}$ ($Q_c^S > 10^8$), as indicated by the vertical gray line, which corresponds to the nominal parameters of the measured device.

The qubit-resonator coupling geometry presented in Fig. 1(b) relies on the use of an aperture in one of the metal layers. Radiation fields from an aperture usually constitute spurious loss and cross-talk mechanisms, but in our case, this effect is mitigated by the proximity of the opposite superconducting layer. In fact, our work demonstrates that we can put these fields to a good use: mediating the coupling between the planar qubit and multilayer resonator. This approach can be extended to provide low cross-talk interlayer connections for devices with more than two layers, such as the architecture proposed in Ref. [38].

VI. CONCLUSIONS AND PERSPECTIVES

We implemented a multilayer superconducting device for quantum information processing that combines the benefits inherent to the precise geometry control of 2D microfabrication with those of the coherence in 3D qubits and resonators. In particular, the qubit-resonator mode

couplings can be precisely adjusted. We believe that the quality of the measured coherence in the present work results from the confinement of electric fields within the vacuum gap separating lithographically defined layers. The design principles illustrated by our work can be extended to devices with more than two layers, each layer corresponding to a specific function: qubits, control lines, resonators, amplifiers, etc. In particular, the aperture-based coupling method introduced here can be generalized to interlayer coupling in such multilayer devices. Furthermore, the TEM mode structure and the separation of layers provides a favorable geometry for hybrid systems, such as spin ensembles with cavities [43,44], spin qubits with magnetic contacts [45], or nanowire qubits [46,47].

ACKNOWLEDGMENTS

We thank T. Brecht, M. Reagor, C. Wang, S. Shankar, and M. Rooks, for valuable discussions. Facilities use was supported by YINQE and NSF MRSEC DMR 1119826. This research was supported by ARO under Grants No. W911NF-14-1-0011 and No. N0014-14-1-0338, and ONR under Grant No. N0014-14-1-0338.

APPENDIX A: DESIGN DETAILS

1. System Hamiltonian

If we expand the Josephson junction cosine potential to fourth order, apply the rotating wave approximation, and limit the Hilbert space of the transmon mode to the first two levels [32], then the effective device Hamiltonian is

$$\mathcal{H}/\hbar = \frac{\omega_q}{2}(1+\sigma_z) + \omega_s a^\dagger a + \omega_r b^\dagger b - \frac{1}{2}(1+\sigma_z)(\chi_{qs} a^\dagger a + \chi_{qr} b^\dagger b) - \chi_{sr} a^\dagger a b^\dagger b, \tag{A1}$$

where a and b are storage and readout bosonic operators, respectively, and σ_z is a qubit Pauli operator. The storage-readout cross Kerr is $\chi_{sr} \approx \chi_{qs}\chi_{qr}/\alpha_q$, where α_q is the transmon anharmonicity.

2. *I-O* coupling

Figure 5(a) shows a simulated field profile for the $D^{\parallel}$ mode, where the maximum currents flow parallel to the axis of symmetry of the rings [23]. The orthogonal $D^{\perp}$ mode corresponds to exchanging the field and current maxima and minima.

As illustrated in the inset of Fig. 5(b), two nonmagnetic pins penetrate the sample-holder lid to couple capacitively with the maximal charge densities of the readout above the thinnest ($\theta = 0$) and thickest ($\theta = 180°$) parts of the rings. Owing to the selective coupling due to the spatial mode orthogonality, the nominal readout coupling Q_c^R is 1.8×10^4, while the nominal storage-mode coupling Q_c^S exceeds 10^8.

APPENDIX B: EXPERIMENTAL DETAILS

1. Fabrication

We microfabricate both layers on the same, double-side-polished, c-plane sapphire wafer with thickness of 430 μm. Using a Vistec electron-beam pattern generator (100 kV), we define the WG resonator and qubit in a single lithography step on a PMMA/MAA resist bilayer. We then perform a double-angle Al evaporation (layer thicknesses: 20 and 30 nm) in a Plassys UMS300 at a pressure of 5×10^{-8} Torr. Between these two depositions, an AlOx barrier is formed by thermal oxidation for 6 minutes in a static environment of 85% argon and 15% oxygen at 100 Torr. Chips are diced to 15.5×25.4 mm.

2. Qubit design details

The qubit island inside is connected to the ring by a wire by a wire (thickness: 1 μm) and a 130×700 nm Josephson junction with $E_J/h = 12$ GHz. The value $E_J/E_C = 44$ yields a maximum offset-charge dispersion of 30 kHz.

3. Sample holder

The chips are placed inside the bottom piece on ledges that are machined in the Al walls. The sample-holder top piece has four legs which use indium to secure the chips against the sample-holder bottom.

4. Measurement setup

An aluminium and permalloy shield protect the sample from stray magnetic fields. The SMA input lines have thermalized cryogenic attenuators (20, 10, and 30 dB) at the 4 K, 0.1 K, and 15 mK stages of a Cryoconcept DR-JT-S-200-10 dilution refrigerator, respectively. The sample-holder output connects to a Josephson parametric converter (JPC) amplifier [31] through two Pamtech cryogenic circulators (4–8 GHz) and superconducting NbTi-NbTi coaxial cables. The JPC serves as a phase-preserving amplifier which operates near the quantum limit with a gain of 21 dB over a bandwidth of 5.6 MHz. Two circulators (4–8 GHz) together with two low-pass filters—a K&L multisection low pass (12 GHz cutoff) and a box-type Eccosorb CR-110 filter—serve to isolate the JPC from the following Low-noise Factory HEMT with 40 dB of gain. We find an noise rise figure of 8 dB for the amplification chain, indicating that the observed noise at room temperature is ~90% amplified quantum fluctuations, though the total quantum efficiency of the measurements is lower due to losses. At room temperature, a 30 dB Miteq amplifier further amplifies the signal and feeds it into a standard heterodyne microwave interferometer operating at an intermediate frequency of 50 MHz. An analog-to-digital

converter records the mixed-down output signal together with a mixed-down reference of the input signal. Combining the output and reference signals accounts for any phase drift in the readout control generator.

At room temperature, we use a Tektronix 5014C arbitrary waveform generator, an Agilent E8257D vector generator, and several Vaunix Lab Brick generators to generate the qubit and cavity tones.

APPENDIX C: DETAILS OF QUBIT AND STORAGE-MODE COHERENCE MEASUREMENTS

The qubit parameters are in the convenient regime for continuous state monitoring, where the dispersive shift and output coupling rate are nearly equal. From quantum jump measurements, not presented here, we infer a qubit excited-state population below 4%.

1. Qubit coherence

The inset of Fig. 6 shows the Ramsey coherence signal of the qubit which decays with a Gaussian envelope and a time constant $T_2^R = 8\ \mu$s. Since this Gaussian envelope is indicative of low-frequency noise, we use dynamical decoupling techniques to access the intrinsic qubit coherence. A Carr-Purcell-Meiboom-Gill (CPMG) protocol, following the approach and pulse-train calibrations of Ref. [48], shift the maximum of the longitudinal noise susceptibility of the qubit to higher frequencies. Figure 6 shows the increase of the dynamically decoupled coherence time T_2^N as a function of the number of CPMG pulses. The improvement of T_2^N beyond T_1 confirms the dominance of low-frequency noise. The Gaussian envelope, indicative of low-frequency noise, could be the result of mechanical vibrations and/or offset charge drifts.

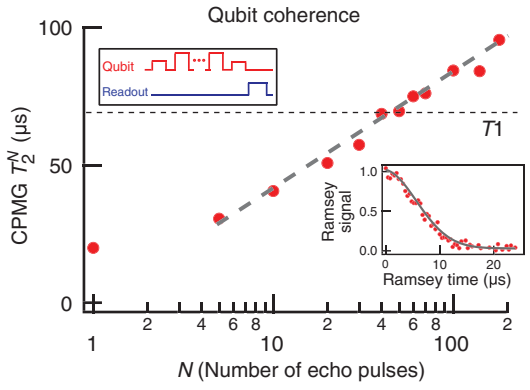

FIG. 6. We measure $T_2^R = 8\ \mu$s (inset) and $T_2^E = 20\ \mu$s. By dynamically decoupling the qubit from low-frequency noise we observe an order-of-magnitude improvement in the coherence time of the aperture transmon exceeding T_1. The dashed line is a guide for the eye.

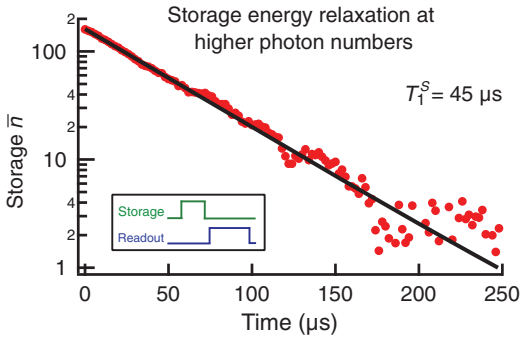

FIG. 7. Using the dispersive cross-Kerr interaction with the readout mode $\chi_{sr}/2\pi = 0.25$ kHz (pulse sequence in inset), we measure a storage lifetime $T_1^S = 45\ \mu$s for $\bar{n} > 10$ photons.

2. Storage-mode lifetime

To measure the storage T_1^S at a photon level of 10–200, we use a dispersive readout of the storage ring-down (see Fig. 7), which, in our case, is more sensitive than a direct-amplitude decay measurement. The dispersive readout is based on the cross-Kerr frequency shift of the readout mode due to the storage photon occupation. We apply a coherent pulse of 500 μs to excite the storage mode, followed by a low-power tone (duration 250 μs) to probe the readout frequency. The storage photon population decayed exponentially with a lifetime $T_1^S = 45\ \mu$s. The resolution of this dispersive measurement is too low to access the single-photon regime, because of the small ratio (10^{-3}) between the cross-Kerr coupling and the readout linewidth.

3. *I-O* coupling

Over several cooldowns, we progressively decrease the *I-O* coupling by shortening the coupling pin lengths. However, while the overcoupled readout lifetime increases by a factor of two to the value in Table I, the qubit and storage-mode lifetimes, as well as the frequencies and nonlinear coupling strengths, do not change measurably. From this, we place a lower bound on the measured storage coupling $Q_c^S > 10^8$.

APPENDIX D: PHOTON-NUMBER PARITY CALIBRATION WITH QUBIT-STATE REVIVALS

1. Experimental method of parity measurement and calibration

To measure the storage photon-number parity presented in Fig. 4(b), we perform a protocol introduced in Refs. [25,35]. After displacing the storage using a coherent drive, we apply a $\pi/2$ pulse, which activates the qubit-storage cross-Kerr interaction and fully entangles the storage parity with the qubit at a time t_p after the qubit pulse. A second $\pi/2$ pulse maps the parity to the expectation value of the qubit σ_z operator, which is read out

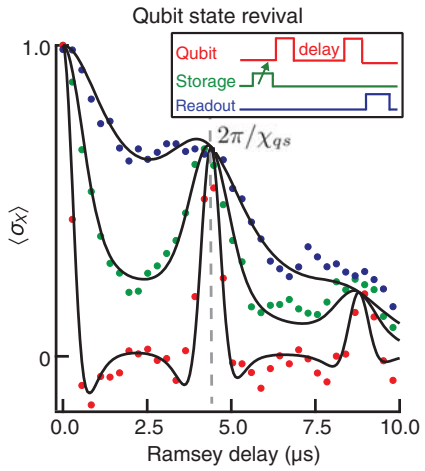

FIG. 8. Calibration of the photon-number parity measurement in the storage is achieved with a qubit-state revival experiment. For small storage-mode displacements $\bar{n}_s \sim 0$ (blue), the decay is dominated by intrinsic qubit decoherence. For increasing displacements, up to $\bar{n}_s = 3$ (red), the apparent increase in decoherence is due to the large qubit-cavity interaction rate, and we observe qubit-state revivals at integer multiples of $2t_p = 2\pi/\chi_{qs}$.

projectively. This is the measurement sequence used for the parity measurement of Fig. 4(b).

This protocol requires calibration of the initial displacement photon number $\bar{n}$ and the parity mapping delay time $t_p = \pi/\chi_{qs}$. To perform the calibration, we displace the WG storage by a short, coherent drive, and then perform a standard qubit T_2 Ramsey experiment, as shown in Fig. 8. Sharp coherence peaks stroboscopically reappear at integer multiples of the cross-Kerr interaction period $2\pi/\chi_{qs}$, indicating the value of $\chi_{qs}/2\pi = 0.25$ MHz. From a global fit to the theory [Eq. (D1)] over all displacement amplitudes, we calibrate the corresponding storage photon numbers $\bar{n}$.

2. Calibration theory

During the measurement, the readout mode remains unpopulated, and we can ignore its contribution to the system Hamiltonian from Eq. (A1). In the rotating frame of the storage and qubit, the system Hamiltonian takes the form

$$H/\hbar = -\chi_{qs} a^\dagger a |e\rangle\langle e|.$$

For a system starting in the ground state, the calibration Ramsey signal of Fig. 8 obeys the following form as a function of time t:

$$\langle\sigma_z\rangle = \frac{1}{2} e^{-(t/T_2)^2 - \bar{n}[1-\cos(\chi_{qs}t)]} \{\cos[\bar{n}\sin(\chi_{qs}t) + \Delta t] - 1\}, \tag{D1}$$

where $\bar{n}$ is the average photon number in the storage mode, Δ is the pulse detuning from the qubit frequency, and $1/T_2$ is the incoherent dephasing rate.

APPENDIX E: SIMULATION OF QUBIT-CAVITY COUPLING

We numerically simulate the qubit design shown in Fig. 2(a) for various qubit-position angles θ using a HFSS, and for each simulation, we extract the effective coupling rate g. We treat the Josephson junction as a lumped, linear inductor in each HFSS eigenmode simulation and find the linearized mode frequencies to construct the linearized system Hamiltonian [32]. To treat the perturbing effect of the nonlinear Josephson terms in the full Hamiltonian, we first calculate their magnitude using the energy-participation-ratio method [49], which is based on the fields already found in the eigenmode simulation. Second, we numerically diagonalize the full Hamiltonian to find the energy spectrum of the system. From the spectrum, we extract the frequencies and Kerr coefficients of the transmon and the resonator modes; from these, we calculate the coupling rate g.

[1] A. Blais, R.-S. Huang, A. Wallraff, S. M. Girvin, and R. J. Schoelkopf, Cavity quantum electrodynamics for superconducting electrical circuits: An architecture for quantum computation, Phys. Rev. A **69**, 062320 (2004).

[2] A. Wallraff, D. I. Schuster, A. Blais, L. Frunzio, R.-S. Huang, J. Majer, S. Kumar, S. M. Girvin, and R. J. Schoelkopf, Strong coupling of a single photon to a superconducting qubit using circuit quantum electrodynamics, Nature (London) **431**, 162 (2004).

[3] M. H. Devoret and R. J. Schoelkopf, Superconducting circuits for quantum information: An outlook, Science **339**, 1169 (2013).

[4] R. Barends, J. Kelly, A. Megrant, A. Veitia, D. Sank, E. Jeffrey, T. C. White, J. Mutus, A. G. Fowler, B. Campbell, Y. Chen, Z. Chen, B. Chiaro, A. Dunsworth, C. Neill, P. O'Malley, P. Roushan, A. Vainsencher, J. Wenner, A. N. Korotkov, A. N. Cleland, and J. M. Martinis, Superconducting quantum circuits at the surface code threshold for fault tolerance, Nature (London) **508**, 500 (2014).

[5] M. Hofheinz, H. Wang, M. Ansmann, R. C. Bialczak, E. Lucero, M. Neeley, A. D. O'Connell, D. Sank, J. Wenner, J. M. Martinis, and A. N. Cleland, Synthesizing arbitrary quantum states in a superconducting resonator, Nature (London) **459**, 546 (2009).

[6] G. Kirchmair, B. Vlastakis, Z. Leghtas, S. E. Nigg, H. Paik, E. Ginossar, M. Mirrahimi, L. Frunzio, S. M. Girvin, and R. J. Schoelkopf, Observation of quantum state collapse and revival due to the single-photon Kerr effect, Nature (London) **495**, 205 (2013).

[7] L. Bretheau, P. Campagne-Ibarcq, E. Flurin, F. Mallet, and B. Huard, Quantum dynamics of an electromagnetic mode that cannot contain N photons, Science **348**, 776 (2015).

[8] Z. Leghtas, S. Touzard, I. M. Pop, A. Kou, B. Vlastakis, A. Petrenko, K. M. Sliwa, A. Narla, S. Shankar, M. J. Hatridge, M. Reagor, L. Frunzio, R. J. Schoelkopf, M. Mirrahimi, and M. H. Devoret, Confining the state of light to a quantum manifold by engineered two-photon loss, Science **347**, 853 (2015).

[9] M. Mariantoni, H. Wang, T. Yamamoto, M. Neeley, R. C. Bialczak, Y. Chen, M. Lenander, E. Lucero, A. D. O'Connell, D. Sank, M. Weides, J. Wenner, Y. Yin, J. Zhao, A. N. Korotkov, A. N. Cleland, and J. M. Martinis, Implementing the quantum von Neumann architecture with superconducting circuits, Science **334**, 61 (2011).

[10] M. Mirrahimi, Z. Leghtas, V. V. Albert, S. Touzard, R. J. Schoelkopf, L. Jiang, and M. H. Devoret, Dynamically protected cat-qubits: A new paradigm for universal quantum computation, New J. Phys. **16**, 045014 (2014).

[11] M. Reagor, H. Paik, G. Catelani, L. Sun, C. Axline, E. Holland, I. M. Pop, N. A. Masluk, T. Brecht, L. Frunzio, M. H. Devoret, L. Glazman, and R. J. Schoelkopf, Reaching 10 ms single photon lifetimes for superconducting aluminum cavities, Appl. Phys. Lett. **102**, 192604 (2013).

[12] B. Vlastakis, A. Petrenko, N. Ofek, L. Sun, Z. Leghtas, K. Sliwa, Y. Liu, M. Hatridge, J. Blumoff, L. Frunzio, M. Mirrahimi, L. Jiang, M. H. Devoret, and R. J. Schoelkopf, Violating Bell's inequality with an artificial atom and a cat state in a cavity, arXiv:1504.02512.

[13] J. Majer, J. M. Chow, J. M. Gambetta, J. Koch, B. R. Johnson, J. A. Schreier, L. Frunzio, D. I. Schuster, A. A. Houck, A. Wallraff, A. Blais, M. H. Devoret, S. M. Girvin, and R. J. Schoelkopf, Coupling superconducting qubits via a cavity bus, Nature (London) **449**, 443 (2007).

[14] M. A. Sillanpää, J. I. Park, and R. W. Simmonds, Coherent quantum state storage and transfer between two phase qubits via a resonant cavity, Nature (London) **449**, 438 (2007).

[15] A. A. Houck, J. A. Schreier, B. R. Johnson, J. M. Chow, J. Koch, J. M. Gambetta, D. I. Schuster, L. Frunzio, M. H. Devoret, S. M. Girvin, and R. J. Schoelkopf, Controlling the Spontaneous Emission of a Superconducting Transmon Qubit, Phys. Rev. Lett. **101**, 080502 (2008).

[16] M. D. Reed, B. R. Johnson, A. A. Houck, L. DiCarlo, J. M. Chow, D. I. Schuster, L. Frunzio, and R. J. Schoelkopf, Fast reset and suppressing spontaneous emission of a superconducting qubit, Appl. Phys. Lett. **96**, 203110 (2010).

[17] R. Barends, N. Vercruyssen, A. Endo, P. J. de Visser, T. Zijlstra, T. M. Klapwijk, P. Diener, S. J. C. Yates, and J. J. A. Baselmans, Minimal resonator loss for circuit quantum electrodynamics, Appl. Phys. Lett. **97**, 023508 (2010).

[18] A. Megrant, C. Neill, R. Barends, B. Chiaro, Y. Chen, L. Feigl, J. Kelly, E. Lucero, M. Mariantoni, P. J. J. OMalley, D. Sank, A. Vainsencher, J. Wenner, T. C. White, Y. Yin, J. Zhao, C. J. Palmstrom, J. M. Martinis, and A. N. Cleland, Planar superconducting resonators with internal quality factors above one million, Appl. Phys. Lett. **100**, 113510 (2012).

[19] R. Barends, J. Kelly, A. Megrant, D. Sank, E. Jeffrey, Y. Chen, Y. Yin, B. Chiaro, J. Mutus, C. Neill, P. OMalley, P. Roushan, J. Wenner, T. C. White, A. N. Cleland, and J. M. Martinis, Coherent Josephson Qubit Suitable for Scalable Quantum Integrated Circuits, Phys. Rev. Lett. **111**, 080502 (2013).

[20] I. M. Pop, K. Geerlings, G. Catelani, R. J. Schoelkopf, L. I. Glazman, and M. H. Devoret, Coherent suppression of electromagnetic dissipation due to superconducting quasiparticles, Nature (London) **508**, 369 (2014).

[21] A. Bruno, G. de Lange, S. Asaad, K. L. van der Enden, N. K. Langford, and L. DiCarlo, Reducing intrinsic loss in superconducting resonators by surface treatment and deep etching of silicon substrates, Appl. Phys. Lett. **106**, 182601 (2015).

[22] H. Paik, D. I. Schuster, L. S. Bishop, G. Kirchmair, G. Catelani, A. P. Sears, B. R. Johnson, M. J. Reagor, L. Frunzio, L. I. Glazman, S. M. Girvin, M. H. Devoret, and R. J. Schoelkopf, Observation of High Coherence in Josephson Junction Qubits Measured in a Three-Dimensional Circuit QED Architecture, Phys. Rev. Lett. **107**, 240501 (2011).

[23] Z. K. Minev, I. M. Pop, and M. H. Devoret, Planar superconducting whispering gallery mode resonators, Appl. Phys. Lett. **103**, 142604 (2013).

[24] B. R. Johnson, M. D. Reed, A. A. Houck, D. I. Schuster, L. S. Bishop, E. Ginossar, J. M. Gambetta, L. DiCarlo, L. Frunzio, S. M. Girvin, and R. J. Schoelkopf, Quantum non-demolition detection of single microwave photons in a circuit, Nat. Phys. **6**, 663 (2010).

[25] B. Vlastakis, G. Kirchmair, Z. Leghtas, S. E. Nigg, L. Frunzio, S. M. Girvin, M. Mirrahimi, M. H. Devoret, and R. J. Schoelkopf, Deterministically encoding quantum information using 100-photon Schrödinger cat states, Science **342**, 607 (2013).

[26] E. Flurin, N. Roch, J. D. Pillet, F. Mallet, and B. Huard, Superconducting Quantum Node for Entanglement and Storage of Microwave Radiation, Phys. Rev. Lett. **114**, 090503 (2015).

[27] J. Koch, T. M. Yu, J. Gambetta, A. A. Houck, D. I. Schuster, J. Majer, A. Blais, M. H. Devoret, S. M. Girvin, and R. J. Schoelkopf, Charge-insensitive qubit design derived from the Cooper pair box, Phys. Rev. A **76**, 042319 (2007).

[28] High frequency structural simulator (HFSS) from ANSYS, Inc.

[29] F. Lecocq, I. M. Pop, Z. Peng, I. Matei, T. Crozes, T. Fournier, C. Naud, W. Guichard, and O. Buisson, Junction fabrication by shadow evaporation without a suspended bridge, Nanotechnology **22**, 315302 (2011).

[30] C. T. Rigetti, Quantum gates for superconducting qubits, Ph.D. thesis, Yale University, 2009.

[31] N. Bergeal, F. Schackert, M. Metcalfe, R. Vijay, V. E. Manucharyan, L. Frunzio, D. E. Prober, R. J. Schoelkopf, S. M. Girvin, and M. H. Devoret, Phase-preserving amplification near the quantum limit with a Josephson ring modulator, Nature (London) **465**, 64 (2010).

[32] S. E. Nigg, H. Paik, B. Vlastakis, G. Kirchmair, S. Shankar, L. Frunzio, M. H. Devoret, R. J. Schoelkopf, and S. M. Girvin, Black-Box Superconducting Circuit Quantization, Phys. Rev. Lett. **108**, 240502 (2012).

[33] This simulation included observed nonideality in the alignment of the rings.

[34] A. P. Sears, A. Petrenko, G. Catelani, L. Sun, H. Paik, G. Kirchmair, L. Frunzio, L. I. Glazman, S. M. Girvin, and R. J. Schoelkopf, Photon shot noise dephasing in the strong-

dispersive limit of circuit QED, Phys. Rev. B **86**, 180504 (2012).

[35] L. Sun, A. Petrenko, Z. Leghtas, B. Vlastakis, G. Kirchmair, K. M. Sliwa, A. Narla, M. Hatridge, S. Shankar, J. Blumoff, L. Frunzio, M. Mirrahimi, M. H. Devoret, and R. J. Schoelkopf, Tracking photon jumps with repeated quantum non-demolition parity measurements, Nature (London) **511**, 444 (2014).

[36] K. Takahashi, U. Sangawa, S. Fujita, M. Matsuo, T. Urabe, H. Ogura, and H. Yabuki, Packaging using microelectromechanical technologies and planar components, IEEE Trans. Microwave Theory Tech. **49**, 2099 (2001).

[37] L. Harle, Microwave micromachined cavity filters, Ph.D. thesis, University of Michigan, 2003.

[38] T. Brecht, W. Pfaff, C. Wang, Y. Chu, L. Frunzio, M. H. Devoret, and R. J. Schoelkopf, Multilayer microwave integrated quantum circuits for scalable quantum computing, arXiv:1509.01127.

[39] R. W. Heeres, B. Vlastakis, E. Holland, S. Krastanov, V. V. Albert, L. Frunzio, L. Jiang, and R. J. Schoelkopf, Cavity state manipulation using photon-number selective phase gates, arXiv:1503.01496.

[40] J. B. Chang, M. R. Vissers, A. D. Co rcoles, M. Sandberg, J. Gao, D. W. Abraham, J. M. Chow, J. M. Gambetta, M. Beth Rothwell, G. A. Keefe, M. Steffen, and D. P. Pappas, Improved superconducting qubit coherence using titanium nitride, Appl. Phys. Lett. **103**, 012602 (2013).

[41] C. M. Quintana, A. Megrant, Z. Chen, A. Dunsworth, B. Chiaro, R. Barends, B. Campbell, Y. Chen, I.-C. Hoi, E. Jeffrey, J. Kelly, J. Y. Mutus, P. J. J. O'Malley, C. Neill, P. Roushan, D. Sank, A. Vainsencher, J. Wenner, T. C. White, A. N. Cleland, and J. M. Martinis, Characterization and reduction of microfabrication-induced decoherence in superconducting quantum circuits, Appl. Phys. Lett. **105**, 062601 (2014).

[42] Z. Leghtas, G. Kirchmair, B. Vlastakis, R. J. Schoelkopf, M. H. Devoret, and M. Mirrahimi, Hardware-Efficient Autonomous Quantum Memory Protection, Phys. Rev. Lett. **111**, 120501 (2013).

[43] B. Julsgaard, C. Grezes, P. Bertet, and K. Mølmer, Quantum Memory for Microwave Photons in an Inhomogeneously Broadened Spin Ensemble, Phys. Rev. Lett. **110**, 250503 (2013).

[44] S. Putz, D. O. Krimer, R. Amsüss, A. Valookaran, T. Nöbauer, J. Schmiedmayer, S. Rotter, and J. Majer, Protecting a spin ensemble against decoherence in the strong-coupling regime of cavity QED, Nat. Phys. **10**, 720 (2014).

[45] A. Cottet and T. Kontos, Spin Quantum Bit with Ferromagnetic Contacts for Circuit QED, Phys. Rev. Lett. **105**, 160502 (2010).

[46] T. W. Larsen, K. D. Petersson, F. Kuemmeth, T. S. Jespersen, P. Krogstrup, J. Nygard, and C. M. Marcus, A semiconductor nanowire-based superconducting qubit, arXiv:1503.08339.

[47] G. de Lange, B. van Heck, A. Bruno, D. van Woerkom, A. Geresdi, S. Plissard, E. Bakkers, A. Akhmerov, and L. DiCarlo, Realization of Microwave Quantum Circuits Using Hybrid Superconducting-Semiconducting Nanowire Josephson Elements, Phys. Rev. Lett. **115**, 127002 (2015).

[48] J. Bylander, S. Gustavsson, F. Yan, F. Yoshihara, K. Harrabi, G. Fitch, D. G. Cory, Y. Nakamura, J.-S. Tsai, and W. D. Oliver, Noise spectroscopy through dynamical decoupling with a superconducting flux qubit, Nat. Phys. **7**, 565 (2011).

[49] Z. Minev *et al.* (to be published).